

Thermodynamic Structure of the Solar Corona: Tomographic Reconstructions and MHD Modeling

Diego G. Lloveras¹  · Alberto
M. Vásquez^{1,2}  · Federico A. Nuevo^{1,3}  ·
Cecilia Mac Cormack^{1,2}  ·
Nishtha Sachdeva⁴  · Ward Manchester
IV⁴  · Bartholomeus Van der Holst⁴  ·
Richard A. Frazin⁴ 

© Springer

Abstract We carry out a study of the global three-dimensional (3D) structure of the electron density and temperature of the quiescent inner solar corona

✉ D.G. Lloveras
dlloveras@iafe.uba.ar
A.M. Vásquez
albert@iafe.uba.ar
F.A. Nuevo
federico@iafe.uba.ar
C. Mac Cormack
cmaccormack@iafe.uba.ar
N. Sachdeva
nishthas@umich.edu
W. Manchester IV
chipm@umich.edu
B. Van der Holst
bartvand@umich.edu
R.A. Frazin
rfrazin@umich.edu

- ¹ Instituto de Astronomía y Física del Espacio (IAFE), CONICET-UBA, CC 67 - Suc 28, (C1428ZAA) Ciudad Autónoma de Buenos Aires, Argentina
- ² Universidad Nacional de Tres de Febrero (UNTREF). Departamento de Ciencia y Tecnología, Sáenz Peña, Argentina.
- ³ Ciclo Básico Común (CBC), Universidad de Buenos Aires (UBA), Buenos Aires, Argentina
- ⁴ Department of Climate and Space Sciences and Engineering (CLaSP), University of Michigan, 2455 Hayward Street, Ann Arbor, MI 48109-2143, USA

($r < 1.25 R_{\odot}$) by means of tomographic reconstructions and magnetohydrodynamic simulations. We use differential emission measure tomography (DEMT) and the Alfvén Wave Solar Model (AWSoM), in their latest versions. Two target rotations were selected from the solar minimum between **Solar Cycles** (SCs) 23 and 24 and the declining phase of SC 24. We report in quantitative detail on the 3D thermodynamic structure of the core and outer layers of the streamer belt, and of the high latitude coronal holes (CH), as revealed by the DEMT analysis. We report on the presence of two types of structures within the streamer belt, loops with temperature decreasing/increasing with height (dubbed down/up loops), as reported first in previous DEMT studies. We also estimate the heating energy flux required at the coronal base to keep these structures stable, found **to be of order** $10^5 \text{ erg cm}^{-2} \text{ s}^{-1}$, consistently with previous DEMT and spectroscopic studies. We discuss how these findings are consistent with coronal dissipation of Alfvén waves. We compare the 3D results of DEMT and AWSoM in distinct magnetic structures. We show that the agreement between the products of both techniques is the best so far, with an overall agreement $\lesssim 20\%$, depending on the target rotation and the specific coronal region. In its current implementation the ASWsoM model **cannot** reproduce down loops though. Also, in the source region of the fast and slow components of the solar wind, the electron density of the AWSoM model increases with latitude, opposite to the trend observed in DEMT reconstructions.

Keywords: Solar Cycle, Observations; Corona, E; Corona, Structures; Corona, Models; Magnetohydrodynamics

1. Introduction

Being the region where the solar atmosphere plasma is heated to million degree temperatures, the solar wind accelerated, and where impulsive events such as solar flares and coronal mass ejections are energized, observing and modeling of the solar corona are of great relevance to improving our understanding of the Sun-Earth environment. To advance our knowledge of the physics of the solar corona, as well as to enhance and validate three-dimensional (3D) models, information derived from observational data plays a key role. Solar rotational tomography (SRT) is currently the sole observational technique able to provide a quantitative empirical description of the 3D distribution of some fundamental plasma parameters of the solar corona at a global scale.

To study the 3D structure of the quiet-Sun global corona, **the** SRT has proven to be a powerful tool. In SRT, solar rotation is taken advantage of, so that instruments gather time series of images covering all viewing angles of the solar corona. **This poses** an inversion problem to solve for the unknown 3D distribution of specific quantities of the solar corona. Based on extreme ultraviolet (EUV) images, taken in several channels sensitive to different temperatures, differential emission measure tomography (DEMT) allows reconstruction of the 3D distribution of the differential emission measure (DEM). The final product of DEMT is in the form of 3D maps of electron density and temperature, covering the range

of heliocentric heights $\lesssim 1.25 R_{\odot}$. The technique was first developed by Frazin, Vásquez, and Kamalabadi (2009), and first applied to the observational study of coronal structures by Vásquez, Frazin, and Kamalabadi (2009). A recent review on DENT was published by Vásquez (2016). The technique is summarised in Section 2.1.

Non-tomographic studies of localized regions of the quiet-Sun corona have been carried out by means of DEM analysis. Mackovjak, Dzifčáková, and Dudík (2014) used regularized inversion techniques to study characteristic temperatures in the quiet-Sun. López *et al.* (2019) used a parametric method to study EUV dimmings after coronal mass ejections (CMEs) to estimate the coronal mass evacuated by the events. At a global scale, DEM analysis has been used by Morgan and Taroyan (2017) to characterise the evolution of the temperature of the quiet-Sun corona during most of Solar Cycle 24.

The combination of DENT with global magnetic models provides insight into the 3D thermodynamical structure of the global corona. DENT was first combined with a potential field source surface (PFSS) model by Huang *et al.* (2012) and Nuevo *et al.* (2013). More recently, Lloveras *et al.* (2017) combined DENT with PFSS models to study the thermodynamics of the global solar corona in specific magnetic structures for two target rotations selected from the last two solar minimum epochs. Also combining DENT with a PFSS model, Mac Cormack *et al.* (2017) developed a new DENT product that estimates the energy input flux required at the coronal base to maintain stable coronal loops. In this article, DENT is first combined with the magnetic field of a magnetohydrodynamic (MHD) model.

The Alfvén Wave Solar Atmosphere Model (AWSoM) within the Space Weather Modeling Framework (SWMF) is a three-dimensional (3D) physics-based, data-driven MHD model extending from the upper chromosphere to the upper corona and reaching 1 AU and beyond (van der Holst *et al.*, 2010, 2014). The only data input of the model is a magnetogram of the global corona, used as boundary condition for the simulation. As new improvements are implemented, the model is continuously being validated with observations. DENT results were used by Jin *et al.* (2012) and Oran *et al.* (2015) to validate AWSoM results finding an agreement within 50% in density and electron temperature in the low corona. More recently, Sachdeva *et al.* (2019) compared the results of the latest version of AWSoM model with DENT products in a global fashion.

In this work, the AWSoM model is used with two purposes. Firstly, to provide an MHD model of the coronal magnetic field to be used to study the DENT results along magnetic field lines. Secondly, to provide thermodynamic results to be compared with those reconstructed by DENT.

Combining the DENT and AWSoM models, we carry out a detailed quantitative analysis of two target rotations. We selected Carrington rotation (CR)2082 (2009, 05 April through 03 May) during the minimum between SCs 23 and 24 and CR 2208 (2018, 02 September through 29 September) during the end of the declining phase of SC 24. In the case of CR 2082, the DENT analysis is based on data taken by the Extreme UltraViolet Imager Behind (EUVI-B: Wuelser *et al.* 2004) on board the Solar TERrestrial RELations Observatory (STEREO),

while **AWSOM** uses the synoptic magnetogram provided by the Global Oscillation Network Group (GONG: Hill *et al.* 1994). In the case of **CR 2208**, the DENT analysis is based on data taken by the Atmospheric Imaging Assembly instrument (AIA: Lemen *et al.* 2012) on board the Solar Dynamics Observatory (SDO), while **AWSOM** uses the magnetogram provide by the Air Force Data Assimilation Photospheric flux Transport (ADAPT)-GONG model.

Section 2.1 and 2.2 **summarise** the DENT technique and the AWSOM model, respectively. Section 2.3 details the method used to trace the DENT results along the field lines of the magnetic model. Section 2.4 details the method that allows determination of the energy input flux at the coronal base. In Section 3.1 the quantitative detailed DENT analysis of both target rotations is shown, and in Section 3.2 the AWSOM and DENT results are compared. Finally, Section 4 **summarises** and discusses the main conclusions of this analysis, and anticipates further planned work.

2. Methodology

2.1. DENT Reconstructions

As detailed in Section 1, rotations **CR 2082** and **CR 2208** were selected to carry out DENT reconstructions, based on data taken by the STEREO/EUVI-B and SDO/AIA instruments, respectively. The EUVI and AIA data were prepared using the latest processing tools and calibration corrections provided by their teams through the **SolarSoftware** package. In the case of EUVI data, stray-light contamination is removed by deconvolution of the point spread function (PSF), carefully determined for each detector by Shearer *et al.* (2012). In the case of AIA data, we have not yet implemented such a procedure as we were not aware of reliable determinations of their PSF, and we also understand that **stray-light** contamination is expected to be less important for this instrument. A recent study by Saqri *et al.* (2020) indicates that the effect is noticeable in DEM analysis of coronal holes (CHs). That is also the case for DEM analysis of EUVI images. Nonetheless, as shown by Lloveras *et al.* (2017), due to the temporal and spatial binning of the images used in tomography the effect of stray-light removal in DENT products turns out to be mild, being $\lesssim 10\%$ for density products and negligible for temperature products. In the future, we will explore the effect of stray-light removal in AIA images on DENT tomography, which we expect to be smaller than for EUVI images. For this work, we introduced two improvements in the implementation of the DENT technique, as described next.

While in all previous DENT studies **full-disc data were used** to perform tomography, in this work we opt to only use off-limb data. In this way, the smallest scale and brighter coronal features seen on **disc** (most typically in the 171Å band) are not included. This has two implications. Firstly, the fast dynamics that typically **characterises** those structures is absent from the data. Secondly, only half synodic rotation worth of data is needed to constrain the inversion problem for the whole coronal volume. As a result, artifacts induced by coronal dynamics are reduced compared to previous DENT reconstructions.

The solution of the tomographic problem involves inversion of a very large sparse matrix. Such inversion problems are characterised by spurious high-frequency artifacts in the solution, which can be mitigated through regularization techniques (Frazin, 2000). In the case of DMT, all previous efforts used the 2D scheme implemented by Frazin, Vásquez, and Kamalabadi (2009), using a finite difference matrix operator to approximate angular derivatives in both latitude and longitude. Also, new to the present work is the implementation of an expanded 3D regularization scheme, which adds to the previous scheme a finite difference matrix operator to approximate radial derivatives. In this way, the tomographic inversion problem is performed penalizing nonphysical high-frequency artifacts in all three spatial directions. As a result, tomographic reconstructions behave more smoothly close to the radial boundaries of the computational grid when compared to previous reconstructions.

In DMT, the inner corona in the range of heliocentric heights $\lesssim 1.25 R_\odot$ is discretized in a spherical computational grid. The size of the tomographic grid cell (or voxel) is typically set to $0.01 R_\odot$ in the radial direction and 2° in both the latitudinal and longitudinal directions. The cadence of the data time-series is set to 6 hr. The main product of the technique is the local DEM (LDEM) at each voxel, a measure of the temperature distribution of the plasma contained in it. We summarise next the main aspects of DMT required for the analysis of this work.

In a first step, the time series of EUV images is used to solve a solar SRT problem, for each EUV band independently. As a result, the 3D distribution of the so called *filter band emissivity* (FBE) is determined for each band separately. The FBE, an emissivity-type quantity, is defined as the wavelength integral of the coronal EUV spectral emissivity and the telescope passband function of each EUV channel. Line-of-sight (LOS) integration of the FBE provides synthetic images that can be quantitatively compared to the real data in the time series. To find the FBE, the tomographic problem is posed as a global optimisation problem in which the quadratic norm of the difference between all pairs of synthetic and real images is minimised.

Due to unresolved coronal dynamics, tomographic reconstructions exhibit negative values of the reconstructed FBE, or zero when the solution is constrained to positive values (Frazin, 2000; Frazin, Vásquez, and Kamalabadi, 2009). These non-reconstructed voxels are indicated in black colour in the latitude-longitude (Carrington) maps of DMT results in Section 3.

In a second step, the FBE values obtained for all bands in each voxel of the tomographic grid are used to constrain the determination of the local DEM (LDEM) which, as described in Section 1, describes the temperature distribution of the plasma within the individual voxel. Specifically, at each tomographic voxel i , the FBE of the band k is related to the LDEM of the voxel according to

$$\text{FBE}_i^{(k)} = \int dT \text{LDEM}_i(T) \text{TRF}^{(k)}(T), \quad k = 1, \dots, K, \quad (1)$$

where K is the number EUV bands, and $\text{TRF}^{(k)}$ is the *temperature response function* of the k -th detector. In this work, the TRFs are computed based on

the (known) **channel** passband times the coronal emissivity at that temperature (**normalised** by the squared electron density). The emissivity model used here is provided by the latest version of the CHIANTI atomic database and plasma emission model (Del Zanna *et al.*, 2015; Landi *et al.*, 2013).

In this work, data from three EUV bands **were** used: 171, 193 and 211 Å in the case of AIA, and 171, 195 and 284 Å in the case of EUVI. When using data from three bands, a Gaussian model for the LDEM is able to accurately predict the FBEs (Nuevo *et al.*, 2015). In each tomographic voxel, the problem is then reduced to finding the values of the three free parameters of the Gaussian (centroid, standard deviation, and area) that best reproduce the three tomographically reconstructed values of FBE in that voxel.

As the LDEM describes the temperature distribution of the plasma in a specific voxel, it does not deal with different large scale structures, as it may be the case for the DEM describing the plasma along a full LOS. As a result, LDEMs are usually successfully modeled with simpler profiles (such as Gaussian) than those returned by DEM studies constrained by LOS-integrated intensities. Parametric techniques are also used for DEM analysis of narrowband images, such as in the works by Aschwanden and Boerner (2011); Plowman, Kankelborg, and Martens (2013); Del Zanna (2013). Other methods applied to DEM analysis of narrow band images include Monte Carlo Markov **chain** (MCMC) techniques (Schmelz, Christian, and Chastain, 2016), regularized inversion techniques (Hannah and Kontar, 2012), and iterative solvers (Pickering and Morgan, 2019; Morgan and Pickering, 2019) that use the known TRFs of all filters as a functional base. The latter work in particular, introduced a fast iterative solver named **Solar Iterative Temperature Emission Solver**, which can easily be adapted for its use in DENT. We will explore this in the future and compare results with those provided by our parametric technique.

Once the LDEM is determined at each voxel, the LDEM-averaged squared electron density N_m^2 and electron temperature T_m in the voxel can be computed by taking its zeroth and first moments over temperature. More specifically, at the i -th voxel,

$$N_{m,i}^2 = \langle N_e^2 \rangle_i = \int dT \text{LDEM}_i(T), \quad (2)$$

$$T_{m,i} = \langle T_e \rangle_i = \frac{1}{\langle N_e^2 \rangle_i} \int dT T \text{LDEM}_i(T). \quad (3)$$

Next, we define a measure of the accuracy of the LDEM model to predict the tomographic FBEs in each voxel, as

$$R_i \equiv (1/K) \sum_{k=1}^K \left| 1 - \text{FBE}_{i,\text{syn}}^{(k)} / \text{FBE}_{i,\text{tom}}^{(k)} \right|, \quad (4)$$

being the **absolute relative difference** between the tomographic and the synthetic FBEs. The final product of DENT is in the form of 3D maps of the LDEM-averaged quantities $\sqrt{N_m^2}$ and T_m , as well as of the measure R . For a full

description of the DMT technique we refer the reader to Frazin, Vásquez, and Kamalabadi (2009).

2.2. AWSoM Simulations

AWSoM is a three-temperature (accounts for anisotropic, parallel and perpendicular, proton temperatures and isotropic electron temperatures), MHD model of the solar corona and inner heliosphere which provides the 3D distribution of density and temperatures, as well as the 3D magnetic structure and velocity of the solar wind. In this work, we use AWSoM simulated results below $1.25 R_{\odot}$ to correspond to the DMT analysis region.

Heating of the solar corona is addressed by including the non-linear interaction of forward and counter-propagating (reflected) Alfvén waves which results in a turbulent cascade. This dissipated turbulent energy is distributed over anisotropic (parallel and perpendicular) proton temperatures and isotropic electron temperature using theories of linear wave damping and stochastic heating.

The model accounts for both collisional and collisionless electron heat conduction and does not use ad-hoc heating functions. The extended MHD equations including radiative cooling, heat conduction and wave turbulence within AWSoM (van der Holst *et al.*, 2014) are solved using the Block-Adaptive Tree Solarwind Roe-type Upwind Scheme (BATS-R-US, Powell *et al.*, 1999; Tóth *et al.*, 2012).

In a previous version of the model, the cascade time of the major wave was used to determine the wave damping rate (Chandran *et al.*, 2011; van der Holst *et al.*, 2014). In its present version, the energy partitioning is improved by using the Alfvén wave number associated with the damping rate as determined by the critical balance condition, which uses the cascade time of the minor wave (Lithwick, Goldreich, and Sridhar, 2007). This leads to more electron heating and less solar wind acceleration (van der Holst, 2019).

The inner boundary of AWSoM is located at the base of the transition region (at $\approx 1.0 R_{\odot}$). In reality, the thin transition region (TR) has steep gradients in temperature and density as a result of the balance between coronal heating, heat conduction, and radiative losses. To resolve these gradients in a global model would require excessive numerical resources. As described in Lionello, Linker, and Mikić (2009) and Sokolov *et al.* (2013), the TR is artificially broadened to be resolved with a finest grid resolution of $0.001 R_{\odot}$. To ensure that the base of the TR is not affected by chromospheric evaporation we overestimate the density at the inner boundary, $N_e = N_i = N_{\odot} = 2 \times 10^{17} \text{ m}^{-3}$, corresponding to the isotropic temperature values, $T_e = T_i = T_{i\parallel} = T_{\odot} = 50,000 \text{ K}$, where the subscripts represent electrons and ions. The upper chromosphere is required to extend radially for the density to fall rapidly to correct (lower) values (Lionello, Linker, and Mikić, 2009). At this level, the radiative losses are sufficiently low so that the temperature can increase monotonically with height and form the transition region. Since the broadening of the transition region pushes the corona outwards, the AWSoM model achieves coronal conditions at a height $\approx 1.05 R_{\odot}$, below which results cannot then be compared to coronal tomographic reconstructions.

To drive the AWSoM model, estimates of the photospheric magnetic field of the Sun are the main input. Synoptic magnetograms are used to specify the

initial and the boundary conditions of the magnetic field. We use the PFSS model to extrapolate the 3D magnetic field (from the 2D photospheric magnetic field maps) using spherical harmonics. The source surface is taken to be at $2.5 R_{\odot}$. GONG provides synoptic **full-disc** surface maps of the radial magnetic field component of the Sun. However, since the polar regions are not well observed from the ecliptic, GONG estimates the polar fields by fitting a polynomial to neighboring observed latitudes, which might lead to inaccuracies. An improvement over these maps is provided by the **ADAPT** model (Worden and Harvey, 2000), which creates synchronic-synoptic maps by incorporating supergranulation, meridional circulation, and differential rotation. These maps provide a physics-based description of the unobserved polar magnetic fields (Arge *et al.*, 2010; Henney *et al.*, 2012). In this work, we use the GONG synoptic map as input for **CR 2082** (ADAPT-GONG maps are unavailable for **CR 2082**) and the ADAPT-GONG global magnetic field map for **CR 2208**. Based on results from previous efforts, for **CR 2082** the magnetic field from the GONG map is scaled up by a factor of 1.85 for weak fields ($B_r < 5$ G), while no modification is applied in the case of the ADAPT-GONG map for **CR 2208**. The AWSoM steady-state simulation set-up and input parameters for both rotations are described below.

To account for the energy partitioning between electrons and protons, based on Chandran *et al.* (2011), we set the stochastic heating exponent equal to 0.21 and the amplitude equal to 0.18, for both rotations. The boundary condition for Alfvén wave energy is given by the poynting flux S_A of the outgoing wave, $(S_A/B)_{\odot} = 1.1 \times 10^6 \text{ W m}^{-2} \text{ T}^{-1}$ and $1.0 \times 10^6 \text{ W m}^{-2} \text{ T}^{-1}$ for **CR 2082** and **CR 2208**, respectively, with B_{\odot} being the field strength at the inner boundary. The correlation length of the Alfvén waves is set to, $L_{\perp} \sqrt{B} = 1.5 \times 10^5 \text{ m} \sqrt{T}$, where L_{\perp} is transverse to the magnetic field direction.

The computational domain of the solar corona extends from 1 to $24 R_{\odot}$. The **adaptive spherical grid has a finer resolution near the Sun**, and increases outward with the z-axis aligned with the rotation axis in **heliographic rotation** coordinates. The **adaptive mesh refinement** (AMR) resolves the angular cell size to 1.4° between $1 - 1.7 R_{\odot}$ and to 2.8° outside this radius range. The solar corona component uses about 3 million cells on $6 \times 8 \times 8$ grid blocks (for **CR 2208**) and $6 \times 4 \times 4$ grid blocks for **CR 2082**. Local time stepping is used to speed up the steady state convergence. The AWSoM simulation of the solar corona for solar minimum conditions represented by **CR 2082** and **CR 2208** are compared to the DMT in the results section.

2.3. Tracing Results Along Magnetic Field Lines

To determine the electron density and temperature along individual magnetic field lines, first both the thermodynamic results and the magnetic field obtained with the AWSoM model were interpolated into the DMT grid. Then, the geometry of the field lines is determined by numerical integration of the first order differential equations $dr/B_r = r d\theta/B_{\theta} = r \sin(\theta) d\phi/B_{\phi}$, both inwards and outwards, from the specified 3D coordinates of a starting point. In order to evenly sample the whole volume spanned by the DMT reconstructions, one starting point is selected at the center of each tomographic cell at 6 uniformly

spaced heights, ranging from 1.025 to $1.225 R_{\odot}$, and every 2° in both latitude and longitude, for a total of 97,200 starting points.

For analysis purposes, the traced magnetic field lines are classified as open or closed according to their full geometry. Each closed field line is further classified as “small” or “large”, according to its coronal length L being respectively smaller or larger than the median value of the whole population, which is $\text{Md}(L) \approx 0.5 R_{\odot}$ for both rotations. Finally, each closed magnetic field line is separated in its two “legs”, defined as the two segments that go from each of its two footpoints (i.e. their location at $r = 1 R_{\odot}$) to its apex (i.e. the location of maximum height).

At this stage, DENT and AWSOM products are traced along open and closed magnetic field lines. Once the field line geometry is computed **with** high spatial resolution, only one sample point per tomographic cell is kept (the median one). As a result, for each field line one data point per tomographic cell is obtained. This approach was first used by Huang *et al.* (2012) to study temperature structures in the solar minimum corona and by Nuevo *et al.* (2013) to expand that analysis to rotations with different level of activity.

For each open field line and for each closed field leg, an exponential fit was applied to the electron density data points and a linear fit applied to the electron temperature data points. For DENT, the data points used are $\sqrt{N_m^2}(r)$ and $T_m(r)$, and in case of the AWSOM models the data points used are $N_e(r)$ and $T_e(r)$. The exponential and linear fit equations are described by

$$\sqrt{N_m^2} = N_0 \exp[-(h/\lambda_N) / (r/R_{\odot})], \quad (5)$$

$$T_m = T_0 + a h, \quad (6)$$

where $h \equiv r - 1 R_{\odot}$ is the coronal height measured from the photosphere. In the electron density fit, $\lambda_N [R_{\odot}]$ is the density scale height and $N_0 [\text{cm}^{-3}]$ is the electron density at the footpoint ($h = 0$) of the loop. In the electron temperature fit, $a [\text{MK}/R_{\odot}]$ is the slope and $T_0 [\text{MK}]$ is the electron temperature at the footpoint of the loop. The slope a estimates the radial gradient of the electron temperature along the loop, which we denote as $a = \nabla_r T_m$ hereafter, with $\nabla_r \equiv \mathbf{e}_r \cdot \nabla$ being the radial derivative operator and \mathbf{e}_r the heliocentric radial unit vector.

In the case of the electron density, the fitted function corresponds to the isothermal hydrostatic equilibrium solution, allowing for variation of the solar gravitational acceleration with height. This choice of function provides a straightforward means to directly compare the observed coronal thermodynamical state with the hydrostatic solution.

Coronal magnetic structures for which temperature increases/decreases with height (in the inner corona) were dubbed as up/down loops by Huang *et al.* (2012) and Nuevo *et al.* (2013), who first reported the presence of down loops. As speculated by the authors of those works, down loops can be expected if the heating deposition is strongly confined near the coronal base of a magnetic loop. Down loops were first predicted by Serio *et al.* (1981), and later by Aschwanden and Schrijver (2002). In a recent study, Schiff and Cranmer (2016) reproduced both down and up loops by means of numerical simulations, using a 1D steady-state model and considering time-averaged heating rates.

To determine if the leg of a traced field line is of type up or down, we first determine the Pearson correlation coefficient $\rho(T, r)$ between the DENT temperature T_m and the heliocentric height r . We then select field lines for which the temperature is significantly correlated with height by requiring $|\rho(T, r)| > 0.5$. To test the goodness of the fit we perform a chi-squared test (Press *et al.*, 2002) considering the uncertainty of the DENT data, selecting legs for which the fit matches the data with a 90% confidence level. In this way, legs for which the DENT temperature does not show a significant correlation with height, or the linear fit to temperature is weak, are excluded from the analysis. The test is also applied to the density-height data points, to ensure the trend is reasonably represented by the exponential fit. Finally, selected legs are then classified as up or down according to $\nabla_r T_m > 0$ or $\nabla_r T_m < 0$, respectively. The linear fit allows characterization of the variation of T_m with height by means of a characteristic temperature gradient $\nabla_r T_m$ [MK/R_⊙] along each leg. The chi-squared test to evaluate the quality of the fit considers the uncertainty level in the DENT products due to systematic sources (radiometric calibration and tomographic regularization), that Lloveras *et al.* (2017) estimated to be $\Delta T_m \approx 10\%$ and $\Delta \sqrt{N_m^2} \approx 5\%$. In summary, a selected leg must meet three conditions:

- i) The leg must go through at least five tomographic grid cells with reconstructed data, and there must be at least one data point in each third of the range of heights spanned by the leg. This requirement is set to ensure a reasonably spread sample of heights along the leg.
- ii) The DENT temperature and height points must meet $|\rho(T, r)| > 0.5$.
- iii) The confidence level of both the exponential and linear fits must be larger than 90%.

To **characterise** the global thermodynamic state of the inner solar corona in distinct magnetic structures, the DENT and AWSOM results were traced along the magnetic field lines of the latter model. Based on the geometry and size of the loops, as well as on their thermodynamical properties, their legs were classified in four different types:

- Type 0: **closed-small down** with footpoints in the range $|\text{latitude}| < 50^\circ$.
- Type I: **closed-small up** with footpoints in the range $|\text{latitude}| < 50^\circ$.
- Type II: **closed-large up** with footpoints in the range $|\text{latitude}| > 40^\circ$.
- Type III: open with footpoint in the range $|\text{latitude}| > 60^\circ$.

In the case of closed-small field lines, the population of down and up legs becomes comparable for **CR 2082**, so we classify them into the two complementary classes of legs of type 0 (down) and legs of type I (up). In the case of closed-large field lines, down legs are $\lesssim 15\%$ of the population for both rotations. In the case of open field lines, down legs are $\lesssim 10\%$ of the population for both rotations. Hence, the requirement of being up for legs of type II and III is included to select the vastly dominating population in each case. On the other hand, the inclusion of latitude limits for the footpoints in the classification of legs from type 0 through III is purposely set to study the streamer belt in progressively outer layers, as well as to separate the field lines of the high latitude CHs (legs of type III). In Section 3, the results of both the **DENT reconstruction** and **AWSOM model** in the four classes of legs are statistically analysed.

2.4. Energy Input Flux

The high temperature of the corona requires heating mechanisms to compensate for the energy losses. While the vast majority of the existing literature on coronal heating focuses on active regions (ARs), some studies have been dedicated to the heating of quiet-Sun regions. In particular, Mac Cormack *et al.* (2017) developed a new application of the DENT technique to estimate the energy input flux required at the base of quiet-Sun coronal loops to maintain stability. The technique is based on tracing the DENT results along field lines of a global coronal magnetic model, as described in Section 2.3.

Consider a static energy balance for each magnetic flux tube, in which the dominating losses of radiative power E_r and thermal conduction power E_c are compensated by a coronal heating power E_h (Aschwanden, 2004):

$$E_h(s) = E_r(s) + E_c(s), \quad (7)$$

where s is the position along the flux tube and these quantities are in units of $[\text{erg sec}^{-1} \text{cm}^{-3}]$.

The thermal conduction power E_c equals the divergence of the conductive heat flux F_c , i.e. $E_c(s) = [1/A(s)] d[A(s) F_c(s)]/ds$, where $A(s)$ is the cross-sectional area of the magnetic flux tube at position s . Under a quiescent solar corona plasma regime, the conductive flux is assumed to be dominated by the electron thermal conduction, described by the usual Spitzer model (Spitzer, 1962)

$$F_c(s) = -\kappa_0 T(s)^{5/2} \frac{dT}{ds}(s), \quad (8)$$

where $\kappa_0 = 9.2 \times 10^{-7} \text{erg sec}^{-1} \text{K}^{-7/2}$ is the Spitzer thermal conductivity.

In the corona, EUV emission is dominated by collisions of the emitting ions with free electrons, so that the radiative power scales as N_e^2 . The radiative power of an isothermal plasma at temperature T is then computed as $E_r = N_e^2 \Lambda(T)$, where the radiative loss function $\Lambda(T)$ is calculated by means of an emission model. In this work we used the latest version of the atomic database and plasma emission model CHIANTI (Del Zanna *et al.*, 2015). The radiative power in terms of the LDEM is then given by:

$$E_r = \int dT \text{LDEM}(T) \Lambda(T). \quad (9)$$

The energy balance given by Equation 7 is then integrated in the volume of any given coronal magnetic flux tube. Dividing the result by the flux tube area at the coronal base, and making use of the soleidonal condition of the magnetic field, a field line integrated version of that energy balance is found,

$$\phi_h = \phi_r + \phi_c, \quad (10)$$

where the line-integrated flux quantities $\phi_{r,c} [\text{erg sec}^{-1} \text{cm}^{-2}]$ are given by (Mac Cormack *et al.*, 2017):

$$\phi_r = \left(\frac{B_0 B_L}{B_0 + B_L} \right) \int_0^L ds \frac{E_r(s)}{B(s)}, \quad (11)$$

$$\phi_c = \left(\frac{B_0 F_{c,L} - B_L F_{c,0}}{B_0 + B_L} \right), \quad (12)$$

where L is the length of the loop, and B_0 and B_L are the values of the magnetic field at the **footpoint** of the loop in the coronal base, namely $s = 0$ and $s = L$. For any given field line, all quantities in these two expressions can be computed from the DENT results traced along field lines, **of** the AWSoM magnetic field model, through Equations 8-9. Once computed, the quantity ϕ_h can be calculated, which is the energy input flux required at the coronal base of each coronal **field line** to maintain a stable coronal structure.

3. Results

3.1. Tomographic Results

As described in Section 2.1, we carried out DENT reconstructions of the coronal structure for rotations **CR 2082** and **CR 2208** using STEREO/EUVI and SDO/AIA data, respectively. Once the LDEM was determined for each rotation, the square root of the mean value of the electron density squared $\sqrt{N_m^2}$ and the electron mean temperature T_m were computed at each voxel of the tomographic computational grid **using** Equations 2 and 3, and the measure R was calculated **with** Equation 4.

Figures 1 and 2 show latitude-longitude maps of DENT results for both rotations. Three different heights of interest are selected from the tomographic grid, providing also a detailed 3D view of the tomographic results: the lowest height of the tomographic grid ($1.025 R_\odot$), the lowest height where the AWSoM results are fully consistent with coronal conditions ($1.065 R_\odot$), and a middle height of the tomographic grid ($1.105 R_\odot$). Black voxels correspond to non-reconstructed voxels (see Section 2.1). Thick-black curves indicate the open/closed boundaries of the magnetic field of the AWSoM model, detailed in Section 2.2.

Both target rotations are highly axisymmetric, i.e. characterised by a high azimuthal symmetry. Rotation **CR 2082** has two small ARs, both near latitude $+30^\circ$ and around longitudes 50° and 120° (not identified in the NOAA catalog). Rotation **CR 2208** has two ARs, both near latitude $+5^\circ$ and around longitudes 140° and 300° (NOAA 12722, 12721).

The magnetically open and closed regions of the AWSoM model are associated with CHs and the equatorial streamer belt, respectively. The location of the open/closed boundaries derived from **the AWSoM** model quite accurately matches the regions of the DENT maps, which exhibit the strongest latitudinal gradient of both the electron density and temperature.

Figures 1 and 2 show that the DENT reconstruction of the streamer belt is characterised by relatively higher densities and temperatures in comparison to

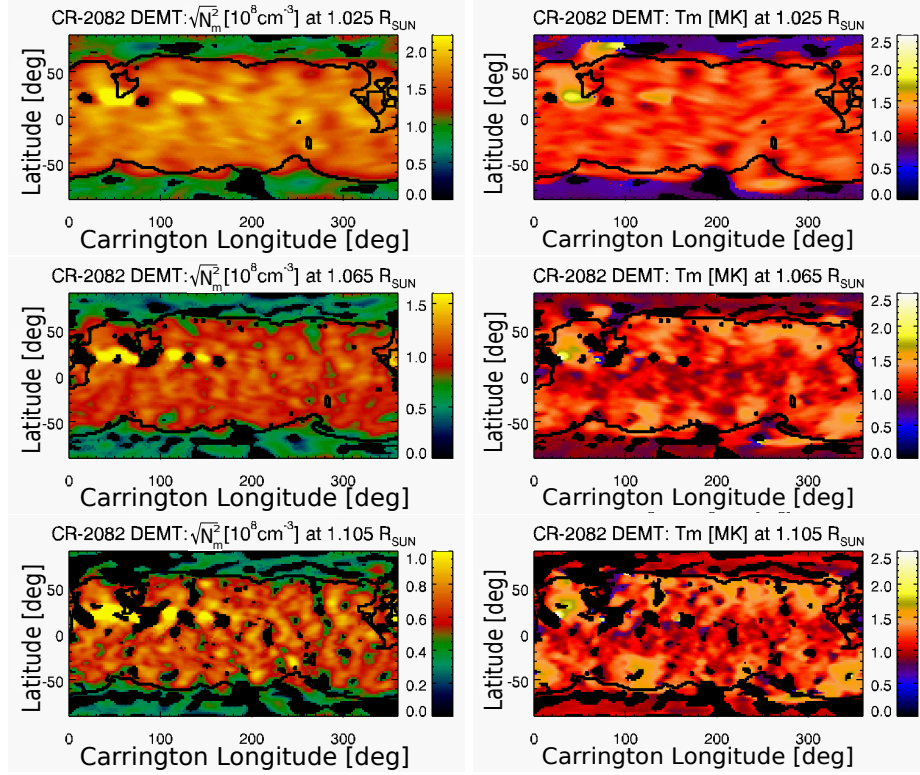


Figure 1. Carrington maps of DENT products $\sqrt{N_m^2}$ (left panels) and T_m (right panels) for CR 2082. Top, middle, and bottom panels show the results at three heliocentric heights, 1.025, 1.065, and 1.105 R_{\odot} respectively. Black voxels correspond to non-reconstructed regions (see text in Section 3.1) and thick-black curves indicate the open/closed boundaries.

the CHs. They also show that the streamer belt region of CR 2082 was denser and colder than that of CR 2208. In the case of CR 2082, which belongs to the deep minimum epoch between SCs 23 and 24, the low latitudes of the streamer belt are characterised by an electron temperature lower than in its mid-latitudes. A similar behaviour is seen in CR 2208, belonging to the end of the declining phase of SC 24 but, having a somewhat less axisymmetric structure, this characteristic is not so obvious. This thermodynamic structure of the streamer has been reported for other solar minimum rotations in previous DENT works (Lloveras *et al.*, 2017; Nuevo *et al.*, 2013; Vázquez, Frazin, and Manchester, 2010).

Latitude-longitude maps of the score R defined by Equation 4 show that the agreement between the tomographic and synthetic FBEs is 5% or better in more than 90% of the reconstructed coronal volume (i.e. where FBEs are non zero), and of order 10% in the rest of the volume. This implies that the LDEM found in each voxel accurately predicts the reconstructed FBEs.

For both rotations, the top panels of Figure 3 show the latitude-longitude location (at heliocentric height $r = 1.105 R_{\odot}$) of all traced field line legs for

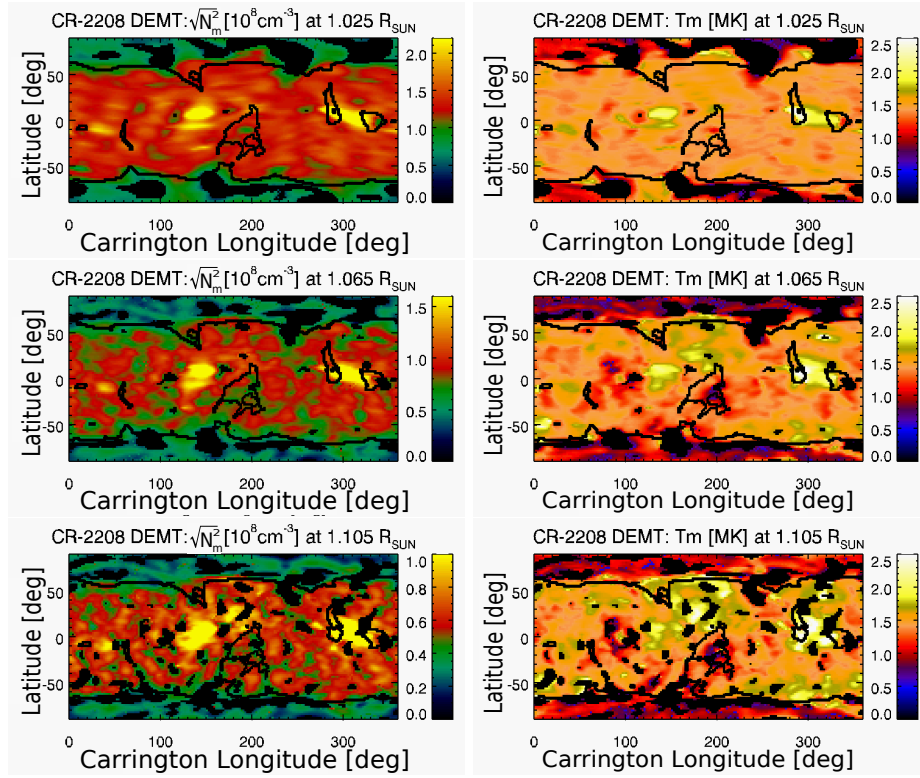


Figure 2. Same as Figure 1 but for **CR 2208**.

which criterion (i) of Section 2.3 is met. Open legs are indicated in **grey colour** and closed ones in **black colour**. Considering the DMT data points and the resulting fits along each leg, the middle panels of Figure 3 show the latitude-longitude location of the subset for which also both criteria (ii) and (iii) of Section 2.3 are met. Using a four-**colour** code, type 0, I, II, and III legs are shown in blue, orange, red, and cyan **colour**, respectively. The bottom panels show histograms of the latitude distribution of the legs of the middle panel, using the same **colour** code. Of the ≈ 44000 legs selected for **CR 2082**, 20% are type 0, 31% are type I, 23% are type II, and 26% type III. On the other hand, of the ≈ 50000 legs selected for **CR 2208**, 10% are type 0, 38% are type I, 27% are type II and 25% type III.

For both rotations, the population of type 0 (**small-closed down**) legs peaks at the core of the streamer belt, around the equator in the case of **CR 2082**, and towards the southern hemisphere in the case of **CR 2208**. This kind of structure was originally found by Huang *et al.* (2012) and their existence was shown to be anti-correlated with the solar activity level around the solar minimum between SCs 23 and 24 by Nuevo *et al.* (2013). Later on, Lloveras *et al.* (2017) showed that equatorial down loops in streamers were also to be found in the deep minimum between SCs 23 and 24. Here, we verify the existence of this type of structure

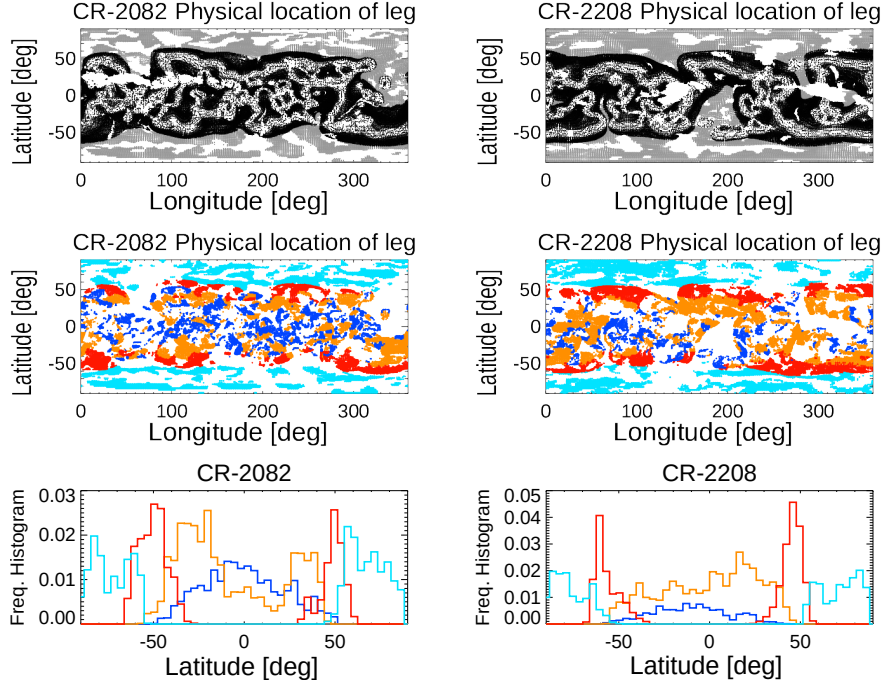


Figure 3. Top panels: latitude-longitude location at heliocentric height $r = 1.105 R_{\odot}$ of all open (grey colour) and closed (black colour) traced field line legs for which criterion (i) of Section 2.3 is met, for CR 2082 (left) and CR 2208 (right). Middle panels: latitude-longitude location of the subset for which both criteria (ii) and (iii) of Section 2.3 are met. The location of type 0, I, II, and III legs is shown in blue, orange, red, and cyan colour, respectively. Bottom panels: frequency histograms of the latitude of the four types of legs of the middle panel.

for the two rotations. The relatively smaller population of down legs seen in CR 2208, as compared to CR 2082, is consistent with the aforementioned results by Nuevo *et al.* (2013). Type I (small-closed-up) legs are present at all latitudes within the streamer belt. Their population peaks in the mid-latitudes of both hemispheres for CR 2082, and in the mid-latitudes of the northern hemisphere for CR 2208. The latitude distribution of legs of type 0 and I in CR 2082 is consistent to the distribution of down and up loops of CR 2081 in the analysis by Nuevo *et al.* (2013), which did not place any limits on the latitude location of the analysed structures.

Type II (large up) legs are mostly very large transequatorial field lines forming the envelope of the streamer belt (the requirement of footpoints located beyond mid-latitudes was included precisely to select this kind of loop). Finally, type III (open) legs populate the high latitude CHs.

Figure 4 shows frequency histograms of $\nabla_r T_m$ for legs of type 0, I, II, and III. The lack of population around values close to zero is due to the requirement $|\rho(T, r)| > 0.5$ which discards quasi-isothermal legs. For both rotations, the median value of the temperature radial gradient is $\text{Md}(\nabla_r T_m) \approx -2.2, +2.3, +2.4$, and $+2.3 \text{ MK}/R_{\odot}$, for legs of type 0, I, II, and III, respectively.

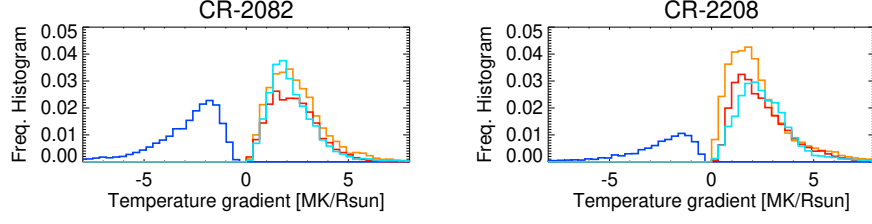


Figure 4. Frequency histograms of the temperature radial gradient for the four types of legs in Figure 3 (using the same colour code) for CR 2082 (left panel) and CR 2208 (right panel).

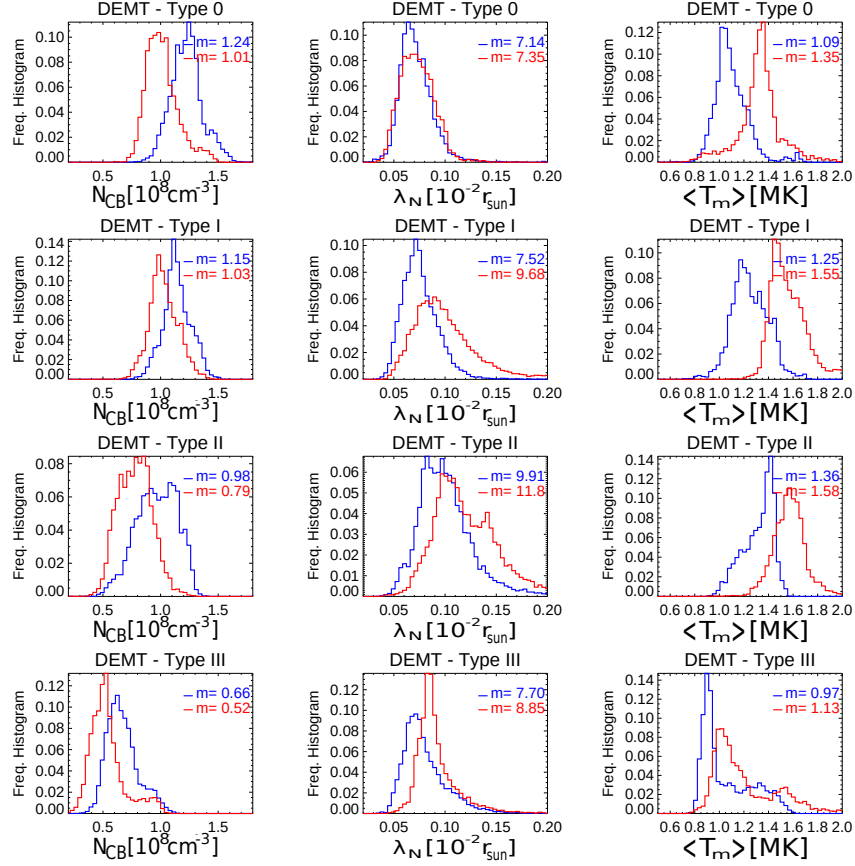


Figure 5. Statistical distribution of DENT results for rotations CR 2082 (blue) and CR 2208 (red) traced along legs of type 0, I, II, and III (from top to bottom), as defined in Section 2.3. From left to right: electron density $N_{CB} \equiv \sqrt{N_m^2}(r = 1.055 R_\odot)$, electron density scale height λ_N , and loop-averaged temperature $\langle T_m \rangle$. In each panel the median value m is indicated.

For both rotations, Figure 5 shows, in a statistical fashion, the DENT results traced along field lines discriminated by leg type. From top to bottom

results are shown for type 0 to type III legs, respectively. From left to right the panels show the statistical distribution of the electron density value $N_{\text{CB}} \equiv \sqrt{N_{\text{m}}^2}(r = 1.055) [\text{cm}^{-3}]$, the scale height λ_N , and the height-averaged (along the leg) electron temperature $\langle T_{\text{m}} \rangle [\text{MK}]$, with the median value m indicated in each plot.

Table 1. Median value (indicated as Md) of the statistical distribution of N_{CB} , λ_N , and $\langle T_{\text{m}} \rangle$ for each coronal type of legs defined in Section 2.3. For **CR 2082**, values are expressed in absolute terms, while for **CR 2208** they are given as a percentual variation relative to the **CR 2082** value in the parentheses.

Type	Md(N_{CB}) [10^8 cm^{-3}]	Md(λ_N) [$10^{-2} \text{ R}_{\odot}$]	Md($\langle T_{\text{m}} \rangle$) [MK]
0	1.24 (-19%)	7.1 (+ 3%)	1.09 (+24%)
I	1.15 (-10%)	7.5 (+29%)	1.25 (+24%)
II	0.98 (-20%)	9.9 (+19%)	1.36 (+16%)
III	0.66 (-21%)	7.7 (+15%)	0.97 (+17%)

Table 1 summarises the results of the quantitative comparative analysis between the two target rotations. For **CR 2082** quantities are expressed as absolute values, while for **CR 2208** they are expressed relative to the corresponding results for **CR 2082**.

Throughout the magnetically closed region of both rotations, type 0, I, and II legs, associated to increasingly outer layers of the equatorial streamer belt, exhibit progressively decreasing coronal base density, increasing density scale height, and increasing electron temperature. In both rotations also, type III legs in the CHs are characterised by sub-MK temperatures, and electron density values of order $\approx 1/2$ of those observed for the type 0 and type I legs in the core of the equatorial streamer. A comparison of the results between the two rotations shows that, compared to **CR 2082**, rotation **CR 2208** was characterised by $\approx 10 - 20\%$ lower values of the electron density at the coronal base, $\approx 5 - 30\%$ larger values of density scale height, and $\approx 15 - 25\%$ larger values of the electron temperature.

In comparing the DENT results obtained for the two selected targets, we highlight they rely on data provided by two different instruments, namely EUVI and AIA for **CR 2082** and **CR 2208**, respectively. To quantify the systematic difference of the DENT products due to the different filter sets of both instruments, Nuevo *et al.* (2015), who were the first to apply DENT to AIA data, analysed a single target using both instruments independently. They found that while the density products are essentially equal, the temperature based on AIA data is systematically 8% larger than the one based on EUVI data, i.e. $T_{\text{m}}^{(\text{AIA})}/T_{\text{m}}^{(\text{EUVI})} \approx 1.08$. Considering this error, Figure 5 and Table 1 indicate that **CR 2208** was characterised by temperatures $\approx 10 - 15\%$ larger relative to **CR 2082** throughout the streamer belt region. As for the electron density products, **CR 2208** was found to be $\approx 10 - 20\%$ less dense than **CR 2082**.

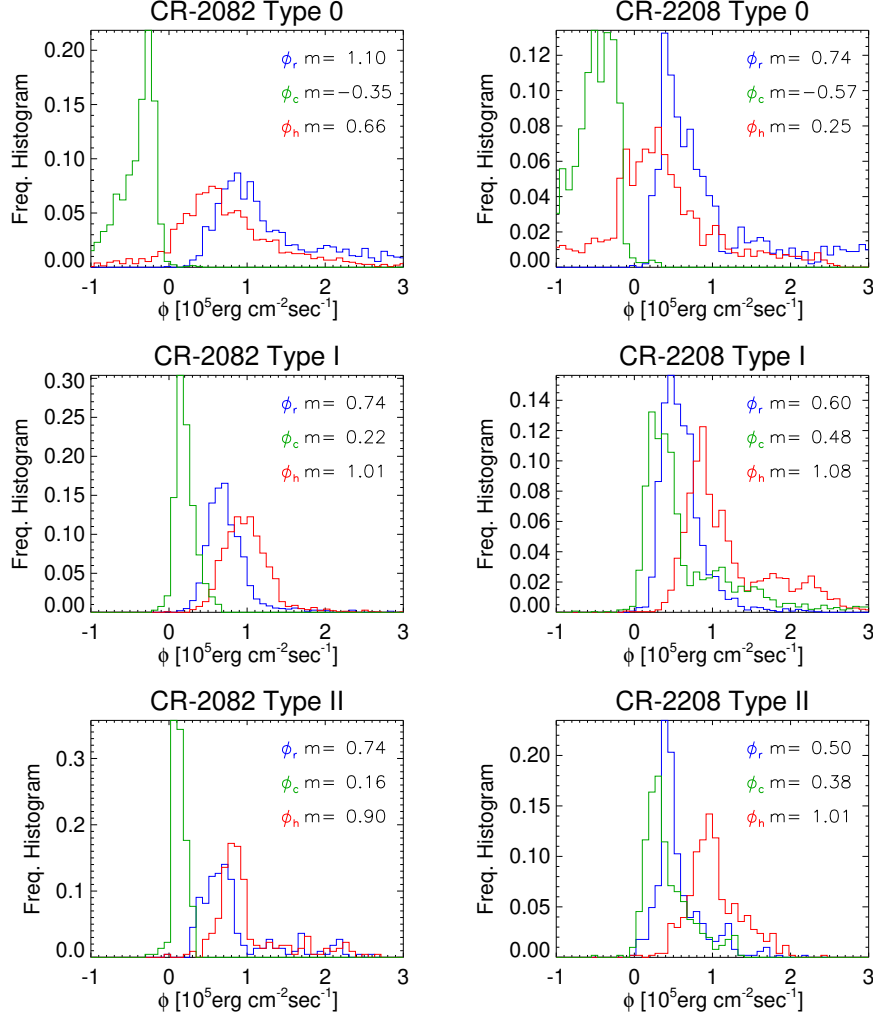


Figure 6. Statistical results of the loop-integrated energy flux quantities ϕ_r , ϕ_c , and ϕ_h in colours blue, red, and green, respectively for CR 2082 (left) and CR 2208 (right). From top to bottom, panels show the results for loops of type 0, I and II, which are loops for which both legs meet the criteria from Section 2.3.

throughout the streamer belt region. These systematic differences are around or beyond the uncertainty level in the DEMT products due to systematic sources (radiometric calibration and tomographic regularization), that Lloveras *et al.* (2017) estimated to be $\Delta T_m \approx 10\%$ and $\Delta \sqrt{N_m^2} \approx 5\%$.

To analyse the loop-integrated energy flux quantities introduced in Section 2.3, we selected closed loops for which both legs have the same sign of the radial gradient of the electron temperature $\nabla_r T_m$. In this way, according to the classification of both legs, each loop was classified as of type 0 (small down loop),

I (small up loop), or II (large up loop). For both target rotations, and for loops of type 0, I, and II, Figure 6 shows the frequency histogram of the loop-integrated energy flux quantities ϕ_r , ϕ_c , and ϕ_h in blue, green, and red colour, respectively.

For both rotations, the value of the loop-integrated radiative power E_r , measured by the quantity ϕ_r , is the largest for loops of type 0. This is due to $E_r \propto N_e^2 \Lambda(T_e)$, with both factors contributing to maximize E_r for loops of type 0. As shown in Figure 5 and Table 1, loops of type 0 are characterised by the largest values of electron density. Also, in the range of sensitivity of the EUVI and AIA instruments, namely 0.5 – 3.0 MK (Nuevo *et al.*, 2015), the radiative loss function $\Lambda(T)$ has a local maximum at $T_c \approx 1$ MK. According to Figure 5, loops of type 0, I, and II are characterised by temperatures that are progressively larger, and farther from T_c , for both rotations.

The sign of the quantity ϕ_c depends on that of the conductive flux F_c . Equations 8 and 12 imply that, by definition, down loops (type 0) and up loops (type I and II) are characterised by $\phi_c < 0$ and $\phi_c > 0$, respectively, as verified in Figure 6.

Adding the radiative and conductive terms, the characteristic energy input flux at the coronal base is in the range $\phi_h \approx 0.5 - 1.5 \times 10^5 \text{ erg cm}^{-2} \text{ s}^{-1}$, depending on the rotation and the type of loop, matching the values reported by Mac Cormack *et al.* (2017). For type 0 loops there is a marginal population characterised by the unphysical result $\phi_h < 0$. As shown by Mac Cormack *et al.* (2017), this affects only the smallest sized loops of the type 0, and it is likely due to emission out of the instrumental sensitivity range. Though accounting for most of the coronal plasma, there surely is additional emission out of the instrumental sensitivity range. As a result, the positive term ϕ_r is most likely underestimated, leading to values $\phi_h < 0$ in loops of type 0, being characterised by $\phi_c < 0$.

3.2. Comparison of the DENT and AWSoM Models

Figure 7 shows Carrington maps of the radial magnetic field B_r for both rotations at $1.005 R_\odot$. Both maps clearly show the large-scale dipolar field, characteristic of solar minimum conditions. Differences between both maps are observed in the sub-polar latitudes, due to the different treatments applied there by the GONG (CR 2082) and the ADAPT-GONG (CR 2208) maps.

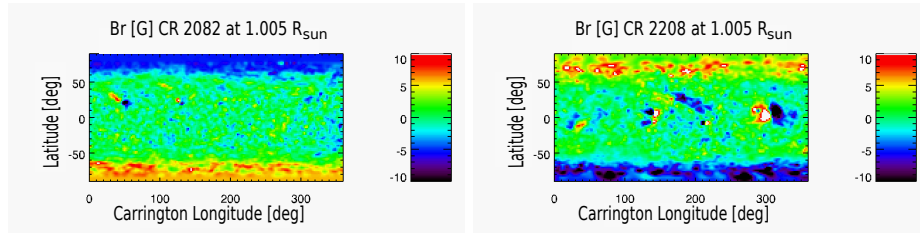


Figure 7. Carrington maps of the radial magnetic field B_r of the AWSoM model at $1.005 R_\odot$ for CR 2082 (left) and CR 2208 (right).

As described in Section 2.2, the AWSoM model includes an artificially thick TR, achieving coronal conditions above height $\approx 1.06 R_{\odot}$. Results for the AWSoM model are shown here above that height. For both target rotations, Figures 8 and 9 show latitude-longitude maps of the AWSoM electron density and temperature. Maps are shown at the two largest heights selected for visualization of the DGMT results in Figures 1 and 2. Thick-black curves indicate the magnetic open/closed boundaries based on the magnetic field of the AWSoM model. Visual inspection of these maps shows that the AWSoM model for both rotations is highly axisymmetric, as the tomographic results.

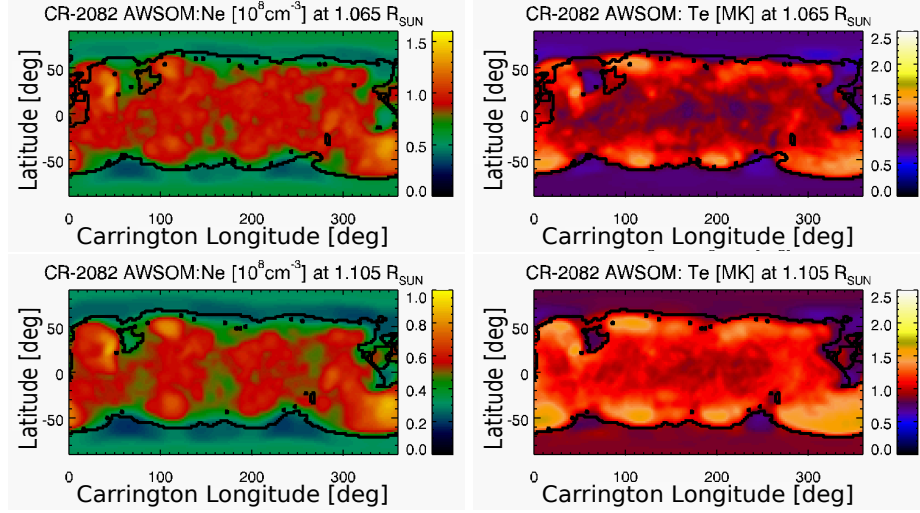


Figure 8. Carrington maps of density (left panels) and temperature (right panels) obtained with AWSoM model at heliocentric heights 1.065 (top panels) and 1.105 R_{\odot} (bottom panels).

When compared to DGMT results (Figures 1 and 2), the latitude-longitude maps of the AWSoM model for heights 1.065 and 1.105 R_{\odot} capture well the denser and hotter equatorial streamer belt surrounded by the less dense and colder CHs. Furthermore, for both rotations, the temperature maps show the low latitudes of the equatorial streamer belt to be characterised by lower temperatures than its mid-latitudes, as also seen in the DGMT results. The latitude-longitude maps of the AWSoM and DGMT results are shown in the same units and scales, so that a visual comparison reveals similar values of electron density and temperature in both models.

Being highly *axisymmetric* rotations, the longitude-averaged latitudinal profile of the results of both models is an informative way to compare their large-scale structure. Such a comparison is shown in Figure 10 at height 1.105 R_{\odot} , with the top panels comparing electron density and *middle panels the electron temperature*. The longitude-averaged latitudinal profile of B_r is shown in the bottom panels. In these longitude-averaged profiles, longitudes containing ARs or low latitude CHs were excluded. In each panel the averaged latitudinal variation for the DGMT model is shown in solid-line style, while the result for the AWSoM

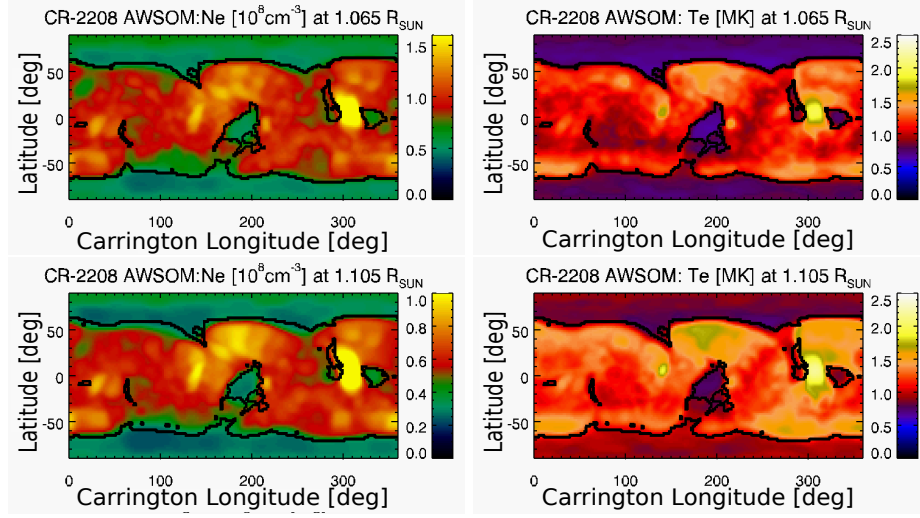


Figure 9. Same as Figure 8 for **CR 2208**.

model is shown in **dashed-line style**. Left panels show the comparison for **CR 2082** (in blue) and right panels for **CR 2208** (in red). In each panel the vertical black lines denote the corresponding longitude-averaged latitude of the open-closed boundary in both hemispheres.

It is worth highlighting several details from Figure 10. Firstly, at most latitudes the overall agreement of the electron density of both models is within $\approx 20\%$ for **CR 2082**, and $\approx 5\%$ for **CR 2208**. The noticeable exception is to be found near the open/closed boundaries of both target rotations, where the disagreement between both models can be up to twice as much. In the case of the electron temperature, for both rotations the models agree within $\approx 15\%$ at all latitudes. Secondly, for both rotations, and for both models, these plots clearly show the relatively lower temperatures **characterising** the low-latitudes of the equatorial streamer belt compared to its mid-latitudes. Thirdly, for both rotations, the latitude of the open/closed magnetic boundary in both hemispheres matches the location of the strongest latitudinal gradient of the DMT electron density. Note this is not the case for the AWSOM model, that shows a minimum density at the open/closed boundary. Lastly, the DMT electron density decreases from the open/closed boundary towards the poles (in both hemispheres of the two rotations), while the AWSOM model shows the opposite trend. For comparison, B_r in the CHs increases from the open/closed boundary towards the poles for **CR 2082**, while showing local maxima around latitudes -75° and $+70^\circ$ in the case of **CR 2208**.

To **characterise** the results of the AWSOM model in distinct magnetic structures, its results for electron density and temperature were traced along its magnetic field lines. For each field line leg, the results were then fit to Equations 5 and 6, considering only data points above heliocentric height $1.055 R_\odot$. We then classified the traced legs into types I, II, and III, according to the criteria

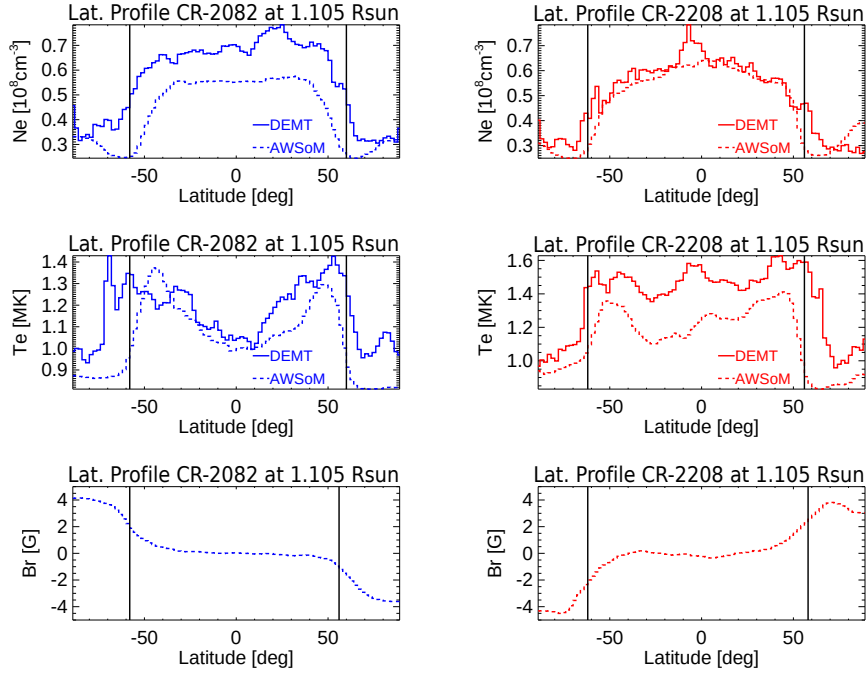


Figure 10. Longitude-averaged latitudinal variation of the electron density (top panels), electron temperature (middle panels), and radial magnetic field B_r (bottom panels), for rotations **CR 2082** (blue colour, left panels) and **CR 2208** (red colour, right panels) at 1.105 R_{\odot} . Dashed and solid lines indicate AWSOM and DGMT results, respectively. Vertical black lines indicate the longitude-averaged latitude of the open/closed magnetic boundary in both hemispheres.

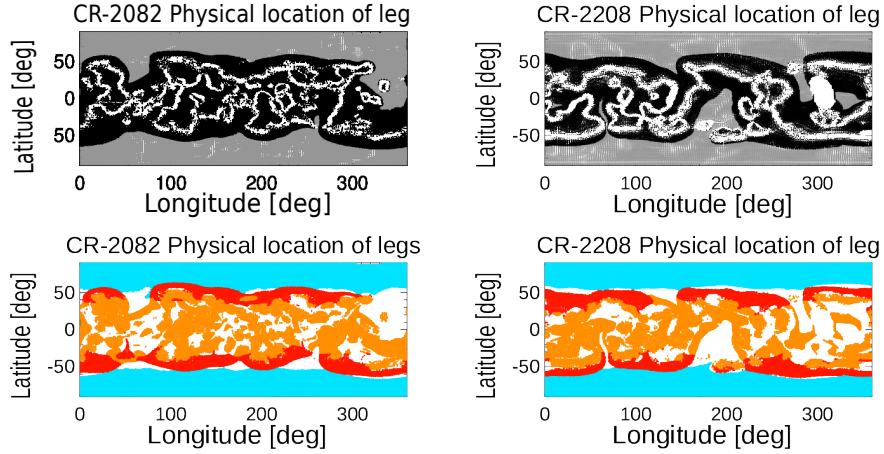


Figure 11. Same as Figure 3, but using the density and temperature of the AWSOM model to classify its legs in types I, II, and III. The model does not exhibit legs of type 0.

described in Section 2.3. Legs of type 0 are not included for AWSoM as it currently can not simulate down loops, as discussed in Section 4.

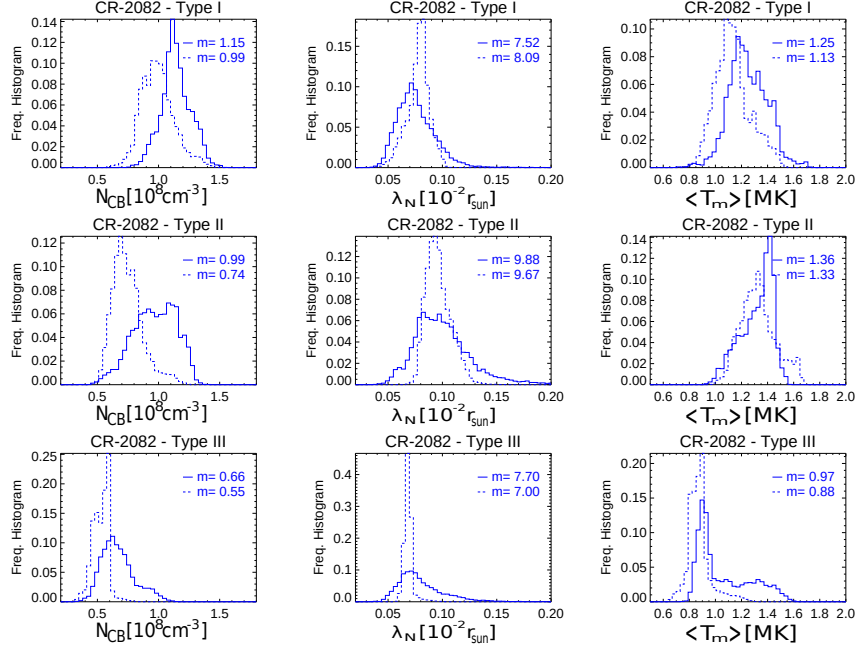


Figure 12. Statistical distribution of the results of the **DEMT reconstruction** (solid line-style) and AWSoM (dashed-line style) traced along legs of type I, II, and III (from top to bottom), as defined in Section 2.3. From left to right: electron density at the lowest coronal height of the AWSoM model $N_e(r = 1.055 R_\odot)$, electron density scale height λ_N , and leg-averaged electron temperature $\langle T_m \rangle$. In each panel the median values m are indicated.

For both target rotations, the top panels of Figure 11 show the latitude-longitude location (at heliocentric height $1.105 R_\odot$) of all traced field line legs for which criterion (i) of Section 2.3 is met. That criterion is adapted here, requiring that at least five voxels of the tomographic grid are threaded by the leg. Open legs are indicated in **grey colour** and closed ones in **black colour**. For each leg, the fits to tomographic temperature and density were applied, as given by Equations 5 and 6. Considering the AWSoM data points and the resulting fits along each leg, the bottom panels of Figure 11 show the latitude-longitude location of the subset for which also both criteria (ii) and (iii) of Section 2.3 are met. Using a three-colour code, type I, II, and III legs are shown in red, magenta, and cyan colour, respectively. This figure can be compared with the corresponding Figure 3 for DEMT results. The AWSoM maps are more densely populated than those of **the DEMT**. This is due to the 3D MHD model having spatially smoother distributions of electron density and temperature than those of **the DEMT**.

For **CR 2082**, Figure 12 shows the statistical distribution of the results of the **DEMT reconstruction** (solid line-style) and AWSoM (dashed line-style) model

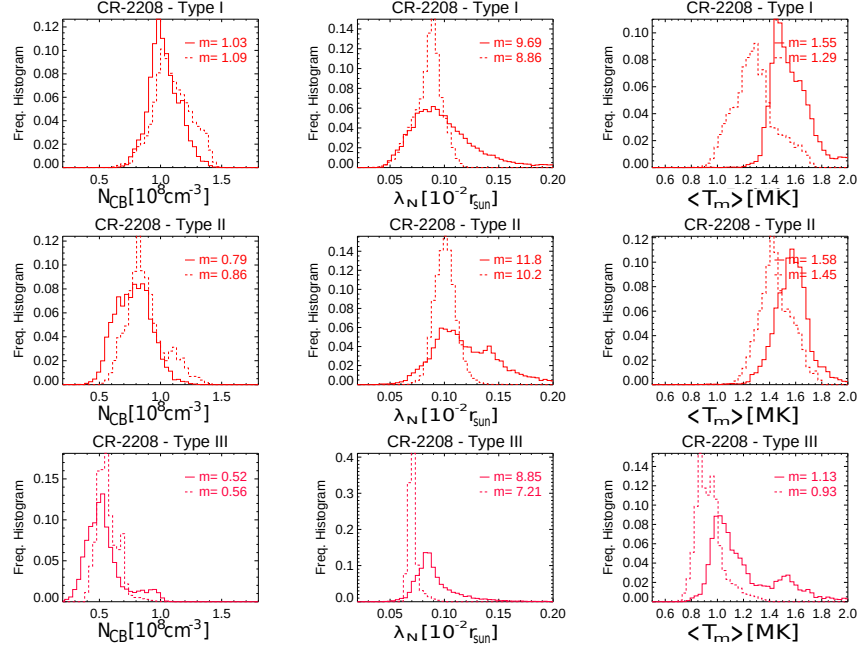


Figure 13. Same as Figure 12 for CR 2208.

traced along legs of type I, II, and III (from top to bottom), as defined in Section 2.3. Figure 13 shows the same analysis for CR 2208.

For the two target rotations, Table 2 summarises the quantitative comparative analysis between the results of the DENT reconstruction and AWSOM model based on the results shown in Figures 12 and 13. The DENT results are expressed as absolute values, while the AWSOM results are informed as a percentual variation relative to the corresponding result for the DENT.

For CR 2082, the median value of the electron density N_{CB} of both models agree within $\approx 10 - 25\%$, depending of the type of leg, with the largest discrepancy found for legs of type II (near the open/closed boundary). The median value of the scale height λ_N agrees within $\approx 10\%$ in all regions. The leg-averaged electron temperature $\langle T_m \rangle$ of both models also agree within 10% in all regions. For CR 2208 the agreement of the median value of N_{CB} and λ_N of both models is within 10%, while median values of $\langle T_m \rangle$ agree within 15%. These detailed results, being consistent with the large-scale comparison provided in Figure 10, show in detail how the AWSOM model performs compared to the DENT in different magnetic structures.

Finally, to provide a graphical comparison of both models across the full range of heliocentric heights covered by the DENT results, Figure 14 shows the average fits of $N_e(r)$ and $T_e(r)$ for legs of type I (red), II (magenta), and III (cyan) for both target rotations. In each panel the DENT and AWSOM results are plotted in solid and dashed line styles, respectively.

Table 2. Median value (indicated as Md) of the statistical distribution of N_{CB} , λ_N , and $\langle T_m \rangle$ for each coronal type of leg defined in Section 2.3. DENT results are expressed in absolute values, while AWSOM results are expressed relative to the corresponding DENT value.

Type	Md(N_{CB}) [10^8 cm^{-3}]	Md(λ_N) [$10^{-2} R_\odot$]	Md($\langle T_m \rangle$) [MK]
CR 2082			
I	1.15 (-14%)	7.5 (+ 8%)	1.25 (-10%)
II	0.99 (-25%)	9.9 (- 2%)	1.36 (- 2%)
III	0.66 (-17%)	7.0 (- 9%)	0.97 (- 9%)
CR 2208			
I	1.03 (+ 6%)	9.7 (- 8%)	1.55 (-17%)
II	0.79 (+ 9%)	11.8 (-14%)	1.58 (- 8%)
III	0.52 (+ 8%)	8.9 (-18%)	1.13 (-18%)

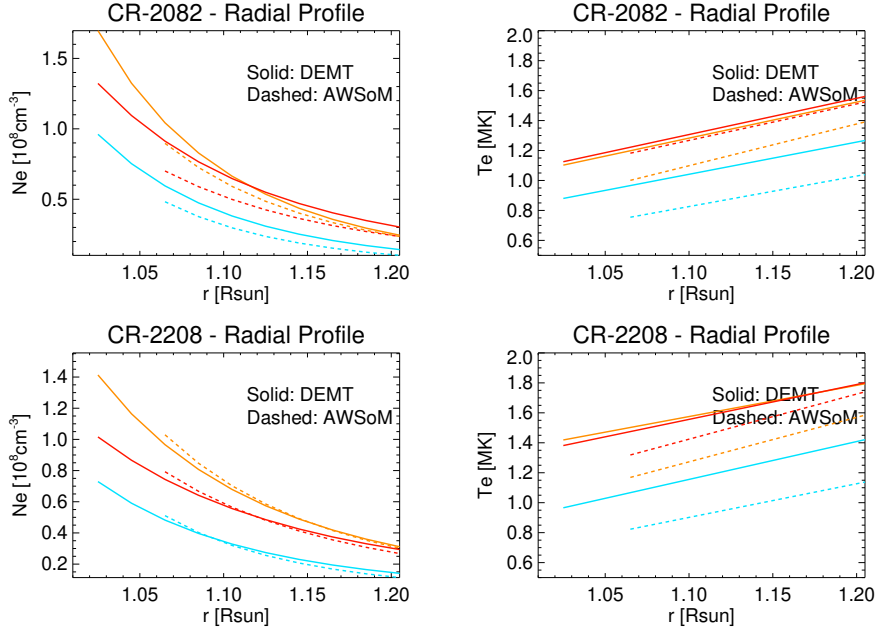


Figure 14. Average fits to $N_e(r)$ (left panels) and $T_e(r)$ (right panels) for legs of type I (orange), II (red), and III (cyan), for **CR 2082** (top panels) and **CR 2208** (bottom panels). Solid lines correspond to DENT results while dashed lines correspond to AWSOM results.

As discussed above, Figure 10 shows that the longitude-averaged latitudinal profile of the DENT electron density in the CHs decreases towards the poles. Figure 15 below shows the longitude-averaged AWSOM radial wind speed V_r at $6 R_\odot$, where all field lines are open. The heliocentric current sheet (HCS)

location is indicated by the minimum of the speed curve. For each rotation, all velocity data points to the south of the HCS position map down to the southern CH in Figures 10. Similarly, all velocity data points to the north of the HCS position map down to the northern CH in Figures 10. This clearly shows an **anticorrelation** between the DMT electron density at low heights and the AWSoM wind speed at larger heights.

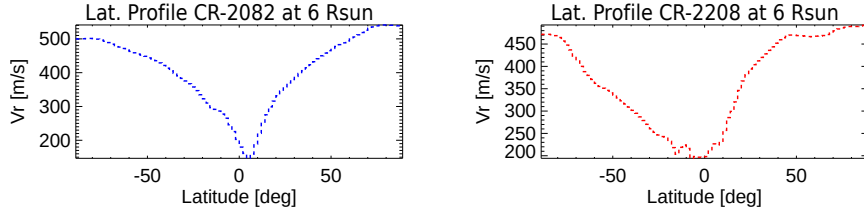


Figure 15. Longitude-averaged latitudinal dependence of the AWSoM model wind speed V_r at $6.0 R_\odot$ for **CR 2082** (left panel) and **CR 2208** (right panel).

4. Discussion and Conclusions

Magnetic field lines of type 0, I, and II were selected to be associated with increasingly outer layers of the equatorial streamer belt (Figure 3). These magnetic structures progressively exhibit decreasing coronal base density, increasing density scale height, and increasing electron temperature, as informed in 3D quantitative detail in Figure 5 and Table 1. For both rotations we find that down legs populate the low latitudes of the streamer belt, while up legs dominate its mid-latitudes. Also, in the case of **CR 2082** the fraction of down legs is significantly larger than for **CR 2208**. These findings are consistent with previous studies by Huang *et al.* (2012) and Nuevo *et al.* (2013). In the case of the latter, they include in their analysis CR 2081, which is a rotation almost identical to our target **CR 2082**. Our results for **CR 2082** compare very well with those of Nuevo *et al.* (2015) and Lloveras *et al.* (2017) for CR 2081. As our study uses the improved version of the DMT technique, such comparison provided a consistency check. For both rotations, type III field lines in the CHs are characterised by sub-MK temperatures, and electron density values of order $\approx 1/2$ of those observed for the type 0 and type I lines in the core of the equatorial streamer.

The energy input flux ϕ_h at the coronal base, required to maintain stable coronal loops, is in the range $\phi_h \approx 0.5 - 1.5 \times 10^5 \text{ erg cm}^{-2} \text{ s}^{-1}$, depending on the rotation and the type of loop, matching the values reported by Mac Cormack *et al.* (2017). Based on spectroscopic data of the EIS instrument in quiet-Sun regions Hahn and Savin (2014) showed that, if the observed non-thermal **broadenings** are assigned to Alfvén waves, their energy flux at the coronal base is estimated to be in the range $\approx 1.5 - 2.5 \times 10^5 \text{ erg cm}^{-2} \text{ s}^{-1}$. A large fraction of the coronal base energy input flux ϕ_h estimated in this work, or even its totality,

could then be accounted for by Alfvén waves (see the discussion in Mac Cormack *et al.* 2017).

The comparison of the results of the AWSoM model to the DENT reconstructions can be summarised as follows. For CR 2082, the electron density of both models agree within $\approx 20\%$ in most regions, while for CR 2208 the agreement is within $\approx 5\%$. The noticeable exception is to be found near the open/closed boundaries of both target rotations, where the disagreement between both models can be up to twice as much. In the case of the electron temperature, both models agree within $\approx 10 - 15\%$. This level of agreement between both models (within or slightly beyond the uncertainty level of the DENT results) is considerably better than that reported in previous works. Jin *et al.* (2012) and Oran *et al.* (2015), who used previous versions of the AWSoM model, reported electron density values differing by $\approx 50\%$ compared to the DENT reconstructions, both in the equatorial streamer and CH regions.

The overall better match of the results of the current version of the AWSoM model compared to DENT reconstructions is partly due to the improved energy partitioning scheme of the model, described in Section 2.2. The simulation of CR 2082 used GONG maps as boundary condition, while the simulation of CR 2208 used the improved ADAPT-GONG maps. This is likely the cause of a more accurate match to the DENT reconstructions in the case of CR 2208.

For both rotations, the AWSoM model reproduces the relatively lower temperatures found by the DENT to characterise the low-latitudes of the equatorial streamer belt compared to its mid-latitudes. On the other hand, while the latitude of the open/closed magnetic boundary in both hemispheres matches the location of the strongest latitudinal gradient of the DENT electron density (physically expected in transitioning from magnetically closed to open regions), this is not the case for the AWSoM model, that shows a minimum density at the open/closed boundary. Also, while the DENT electron density decreases from the open/closed boundary towards the poles (in both hemispheres of the two rotations), as expected in transitioning from the source region of the slow to the fast component of the solar wind, the AWSoM model shows the opposite trend. This behaviour is notoriously opposite to that reported in the AWSoM model version used by Oran *et al.* (2015), in which the electron density decreases from the open/closed boundary towards the poles. These unphysical characteristics of the results of the AWSoM model in the range of low heights analysed here ($r \lesssim 1.2 R_{\odot}$), may be attributed to the less reliable values of B_r provided by both the GONG and ADAPT-GONG maps at subpolar latitudes. This will be investigated in a follow up article focusing on the current deep minimum epoch, during which the large-scale corona shows the simplest possible structure.

Down loops are to be expected if heating is enhanced at the footpoints of coronal structures. Schiff and Cranmer (2016) numerically simulated stable down loops by means of a 1D steady-state model, requiring that the initial population of Alfvén waves is efficiently converted into compressive modes. Mode conversion is favored by the $\beta \gtrsim 1$ condition found to characterise the regions where down loops are observed in DENT analysis (Nuevo *et al.*, 2013). In the AWSoM model, heating is controlled by two key parameters, namely, the Alfvén wave dissipation length, and its reflection coefficient. So far, attempts to reproduce observed down

loops in AWSoM simulations by increasing the reflection coefficient have not been successful.

A detailed empirical description of the 3D thermodynamic structure of the inner corona at a global scale is currently only possible with tomographic techniques, such as [the](#) DMT. Using tomographic results for continuous validation of 3D MHD models is of high relevance for the continued improvement of models. In follow up articles we will carry out the 3D DMT reconstruction and MHD modeling of new target rotations selected from the current solar minimum epoch between SCs 24 and 25, as well as CR 2219 corresponding to the [July 2, 2019](#) total solar eclipse.

Acknowledgments D.G.L. and C.M.C. acknowledge CONICET doctoral fellowships (Res. Nr. 4870) that supported their participation in this research. D.G.L., A.M.V., F.A.N., and C.M.C. acknowledge ANPCyT grant 2016/0221 that partially supported their participation in this research. A.M.V. also acknowledges UBACyT grant 20020160100072BA that partially supported his participation in this research. W.M. and B.v.H acknowledge NSF grant 1663800 that partially supported his participation in this research. W.M. also acknowledges NASA grants NNX16AL12G and 80NSSC17K0686. [The AIA/SDO data used in this study is courtesy of NASA/SDO and the AIA, EVE, and HMI science teams.](#)

Disclosure of Potential Conflicts of Interest: The authors declare that they have no conflicts of interest.

References

- Arge, C.N., Henney, C.J., Koller, J., Compeau, C.R., Young, S., MacKenzie, D., Fay, A., Harvey, J.W.: 2010, Air Force Data Assimilative Photospheric Flux Transport (ADAPT) Model. In: Maksimovic, M., Issautier, K., Meyer-Vernet, N., Moncuquet, M., Pantellini, F. (eds.) *Twelfth International Solar Wind Conference, American Institute of Physics Conference Series* **1216**, 343. DOI. ADS.
- Aschwanden, M.J.: 2004, *Physics of the Solar Corona. An Introduction*. ADS.
- Aschwanden, M.J., Boerner, P.: 2011, Solar Corona Loop Studies with the Atmospheric Imaging Assembly. I. Cross-sectional Temperature Structure. *Astrophys. J.* **732**, 81. DOI. ADS.
- Aschwanden, M.J., Schrijver, C.J.: 2002, Analytical Approximations to Hydrostatic Solutions and Scaling Laws of Coronal Loops. *Astrophys. J. Suppl.* **142**(2), 269. DOI. ADS.
- Chandran, B.D.G., Dennis, T.J., Quataert, E., Bale, S.D.: 2011, Incorporating Kinetic Physics into a Two-fluid Solar-wind Model with Temperature Anisotropy and Low-frequency Alfvén-wave Turbulence. *Astrophys. J.* **743**(2), 197. DOI. ADS.
- Del Zanna, G.: 2013, The multi-thermal emission in solar active regions. *Astron. Astrophys.* **558**, A73. DOI. ADS.
- Del Zanna, G., Dere, K.P., Young, P.R., Landi, E., Mason, H.E.: 2015, CHIANTI - An atomic database for emission lines. Version 8. *Astron. Astrophys.* **582**, A56. DOI. ADS.
- Frazin, R.A.: 2000, Tomography of the Solar Corona. I. A Robust, Regularized, Positive Estimation Method. *Astrophys. J.* **530**, 1026. DOI. ADS.
- Frazin, R.A., Vásquez, A.M., Kamalabadi, F.: 2009, Quantitative, Three-dimensional Analysis of the Global Corona with Multi-spacecraft Differential Emission Measure Tomography. *Astrophys. J.* **701**, 547. DOI. ADS.
- Hahn, M., Savin, D.W.: 2014, Evidence for Wave Heating of the Quiet-Sun Corona. *Astrophys. J.* **795**(2), 111. DOI. ADS.
- Hannah, I.G., Kontar, E.P.: 2012, Differential emission measures from the regularized inversion of Hinode and SDO data. *Astron. Astrophys.* **539**, A146. DOI. ADS.
- Henney, C.J., Toussaint, W.A., White, S.M., Arge, C.N.: 2012, Forecasting F_{10.7} with solar magnetic flux transport modeling. *Space Weather* **10**, S02011. DOI. ADS.

- Hill, F., Fischer, G., Grier, J., Leibacher, J.W., Jones, H.B., Jones, P.P., Kupke, R., Stebbins, R.T.: 1994, The Global Oscillation Network Group Site Survey - Part One. *Solar Phys.* **152**(2), 321. DOI. ADS.
- Huang, Z., Frazin, R.A., Landi, E., Manchester, W.B., Vázquez, A.M., Gombosi, T.I.: 2012, Newly Discovered Global Temperature Structures in the Quiet Sun at Solar Minimum. *Astrophys. J.* **755**, 86. DOI. ADS.
- Jin, M., Manchester, W.B., van der Holst, B., Oran, R., Sokolov, I., Toth, G., Gombosi, T.I., Vourlidas, A., Liu, Y., Sun, X.: 2012, Simulate the Coronal Mass Ejection on 2011 March 7 from Chromosphere to 1 AU. In: *AGU Fall Meeting Abstracts* **2012**, SH33E. ADS.
- Landi, E., Young, P.R., Dere, K.P., Del Zanna, G., Mason, H.E.: 2013, CHIANTI - An Atomic Database for Emission Lines. XIII. Soft X-Ray Improvements and Other Changes. *Astrophys. J.* **763**, 86. DOI. ADS.
- Lemen, J.R., Title, A.M., Akin, D.J., Boerner, P.F., Chou, C., Drake, J.F., Duncan, D.W., Edwards, C.G., Friedlaender, F.M., Heyman, G.F., Hurlburt, N.E., Katz, N.L., Kushner, G.D., Levay, M., Lindgren, R.W., Mathur, D.P., McFeaters, E.L., Mitchell, S., Rehse, R.A., Schrijver, C.J., Springer, L.A., Stern, R.A., Tarbell, T.D., Wuelser, J.-P., Wolfson, C.J., Yanari, C., Bookbinder, J.A., Cheimets, P.N., Caldwell, D., Deluca, E.E., Gates, R., Golub, L., Park, S., Podgorski, W.A., Bush, R.I., Scherrer, P.H., Gumm, M.A., Smith, P., Auker, G., Jerram, P., Pool, P., Soufli, R., Windt, D.L., Beardsley, S., Clapp, M., Lang, J., Waltham, N.: 2012, The Atmospheric Imaging Assembly (AIA) on the Solar Dynamics Observatory (SDO). *Solar Phys.* **275**, 17. DOI. ADS.
- Lionello, R., Linker, J.A., Mikić, Z.: 2009, Multispectral Emission of the Sun During the First Whole Sun Month: Magnetohydrodynamic Simulations. *Astrophys. J.* **690**(1), 902. DOI. ADS.
- Lithwick, Y., Goldreich, P., Sridhar, S.: 2007, Imbalanced Strong MHD Turbulence. *Astrophys. J.* **655**(1), 269. DOI. ADS.
- Lloveras, D.G., Vázquez, A.M., Nuevo, F.A., Frazin, R.A.: 2017, Comparative Study of the Three-Dimensional Thermodynamical Structure of the Inner Corona of Solar Minimum Carrington Rotations 1915 and 2081. *Solar Phys.* **292**(10), 153. DOI. <https://doi.org/10.1007/s11207-017-1179-z>.
- López, F.M., Cremades, H., Balmaceda, L.A., Nuevo, F.A., Vázquez, A.M.: 2019, Estimating the mass of CMEs from the analysis of EUV dimmings. *Astron. Astrophys.* **627**, A8. DOI. ADS.
- Mac Cormack, C., Vázquez, A.M., López Fuentes, M., Nuevo, F.A., Landi, E., Frazin, R.A.: 2017, Energy Input Flux in the Global Quiet-Sun Corona. *Astrophys. J.* **843**, 70. DOI. ADS.
- Mackovjak, Š., Dzifčáková, E., Dudík, J.: 2014, Differential emission measure analysis of active region cores and quiet Sun for the non-Maxwellian κ -distributions. *Astron. Astrophys.* **564**, A130. DOI. ADS.
- Morgan, H., Pickering, J.: 2019, SITES: Solar Iterative Temperature Emission Solver for Differential Emission Measure Inversion of EUV Observations. *Solar Phys.* **294**(10), 135. DOI. ADS.
- Morgan, H., Taroyan, Y.: 2017, Global conditions in the solar corona from 2010 to 2017. *Science Advances* **3**(7), e1602056. DOI. ADS.
- Nuevo, F.A., Huang, Z., Frazin, R., Manchester, W.B., Jin, M., Vázquez, A.M.: 2013, Evolution of the Global Temperature Structure of the Solar Corona during the Minimum between Solar Cycles 23 and 24. *Astrophys. J.* **773**(1), 9. DOI. ADS.
- Nuevo, F.A., Vázquez, A.M., Landi, E., Frazin, R.: 2015, Multimodal Differential Emission Measure in the Solar Corona. *Astrophys. J.* **811**(2), 128. DOI. ADS.
- Oran, R., Landi, E., van der Holst, B., Lepri, S.T., Vázquez, A.M., Nuevo, F.A., Frazin, R., Manchester, W., Sokolov, I., Gombosi, T.I.: 2015, A Steady-state Picture of Solar Wind Acceleration and Charge State Composition Derived from a Global Wave-driven MHD Model. *Astrophys. J.* **806**(1), 55. DOI. ADS.
- Pickering, J., Morgan, H.: 2019, GRID-SITES: Gridded Solar Iterative Temperature Emission Solver for Fast DEM Inversion. *Solar Phys.* **294**(10), 136. DOI. ADS.
- Plowman, J., Kankelborg, C., Martens, P.: 2013, Fast Differential Emission Measure Inversion of Solar Coronal Data. *Astrophys. J.* **771**, 2. DOI. ADS.
- Powell, K.G., Roe, P.L., Linde, T.J., Gombosi, T.I., De Zeeuw, D.L.: 1999, A Solution-Adaptive Upwind Scheme for Ideal Magnetohydrodynamics. *Journal of Computational Physics* **154**(2), 284. DOI. ADS.

- Press, W.H., Teukolsky, S.A., Vetterling, W.T., Flannery, B.P.: 2002, *Numerical recipes in C++ : the art of scientific computing*. ADS.
- Sachdeva, N., van der Holst, B., Manchester, W.B., Tóth, G., Chen, Y., Lloveras, D.G., Vázquez, A.M., Lamy, P., Wojak, J., Jackson, B.V., Yu, H.-S., Henney, C.J.: 2019, Validation of the Alfvén Wave Solar Atmosphere Model (AWSoM) with Observations from the Low Corona to 1 au. *Astrophys. J.* **887**(1), 83. DOI. ADS.
- Saqi, J., Veronig, A.M., Heinemann, S.G., Hofmeister, S.J., Temmer, M., Dissauer, K., Su, Y.: 2020, Differential Emission Measure Plasma Diagnostics of a Long-Lived Coronal Hole. *Solar Phys.* **295**(1), 6. DOI. ADS.
- Schiff, A.J., Cranmer, S.R.: 2016, Explaining Inverted-temperature Loops in the Quiet Solar Corona with Magnetohydrodynamic Wave-mode Conversion. *Astrophys. J.* **831**(1), 10. DOI. ADS.
- Schmelz, J.T., Christian, G.M., Chastain, R.A.: 2016, The Coronal Loop Inventory Project: Expanded Analysis and Results. *Astrophys. J.* **831**(2), 199. DOI. ADS.
- Serio, S., Peres, G., Vaiana, G.S., Golub, L., Rosner, R.: 1981, Closed coronal structures. II - Generalized hydrostatic model. *Astrophys. J.* **243**, 288. DOI. ADS.
- Shearer, P., Frazin, R.A., Hero, I. Alfred O., Gilbert, A.C.: 2012, The First Stray Light Corrected Extreme-ultraviolet Images of Solar Coronal Holes. *Astrophys. J. Lett.* **749**(1), L8. DOI. ADS.
- Sokolov, I.V., van der Holst, B., Oran, R., Downs, C., Roussev, I.I., Jin, M., Manchester, W.B., Evans, R.M., Gombosi, T.I.: 2013, MAGNETOHYDRODYNAMIC WAVES AND CORONAL HEATING: UNIFYING EMPIRICAL AND MHD TURBULENCE MODELS. *apj* **764**(1), 23. DOI. <https://doi.org/10.1088%2F0004-637x%2F764%2F1%2F23>.
- Spitzer, L.: 1962, *Physics of Fully Ionized Gases*. ADS.
- Tóth, G., van der Holst, B., Sokolov, I.V., De Zeeuw, D.L., Gombosi, T.I., Fang, F., Manchester, W.B., Meng, X., Najib, D., Powell, K.G., et al.: 2012, Adaptive numerical algorithms in space weather modeling. *J. Comput. Phys.* **231**(3), 870–903. DOI. <https://doi.org/10.1016/j.jcp.2011.02.006>.
- van der Holst, B.: 2019, to be accepted. *Astrophys. J.*
- van der Holst, B., Manchester, I. W. B., Frazin, R.A., Vázquez, A.M., Tóth, G., Gombosi, T.I.: 2010, A Data-driven, Two-temperature Solar Wind Model with Alfvén Waves. *Astrophys. J.* **725**(1), 1373. DOI. ADS.
- van der Holst, B., Sokolov, I.V., Meng, X., Jin, M., Manchester, I. W. B., Tóth, G., Gombosi, T.I.: 2014, Alfvén Wave Solar Model (AWSoM): Coronal Heating. *Astrophys. J.* **782**(2), 81. DOI. ADS.
- Vázquez, A.M.: 2016, Seeing the solar corona in three dimensions. *Advances in Space Research* **57**, 1286. DOI.
- Vázquez, A.M., Frazin, R.A., Kamalabadi, F.: 2009, 3D Temperatures and Densities of the Solar Corona via Multi-Spacecraft EUV Tomography: Analysis of Prominence Cavities. *Solar Phys.* **256**(1-2), 73. DOI. ADS.
- Vázquez, A.M., Frazin, R.A., Manchester, I. Ward B.: 2010, The Solar Minimum Corona from Differential Emission Measure Tomography. *Astrophys. J.* **715**(2), 1352. DOI. ADS.
- Worden, J., Harvey, J.: 2000, An Evolving Synoptic Magnetic Flux map and Implications for the Distribution of Photospheric Magnetic Flux. *Solar Phys.* **195**(2), 247. DOI. ADS.
- Wuelser, J.-P., Lemen, J.R., Tarbell, T.D., Wolfson, C.J., Cannon, J.C., Carpenter, B.A., Duncan, D.W., Gradwohl, G.S., Meyer, S.B., Moore, A.S., Navarro, R.L., Pearson, J.D., Rossi, G.R., Springer, L.A., Howard, R.A., Moses, J.D., Newmark, J.S., Delaboudiniere, J.-P., Artzner, G.E., Auchere, F., Bougnet, M., Bouyries, P., Bridou, F., Clotaire, J.-Y., Colas, G., Delmotte, F., Jerome, A., Lamare, M., Mercier, R., Mullot, M., Ravet, M.-F., Song, X., Bothmer, V., Deutsch, W.: 2004, EUVI: the STEREO-SECCHI extreme ultraviolet imager. In: Fineschi, S., Gummin, M.A. (eds.) *Telescopes and Instrumentation for Solar Astrophysics, Proc. SPIE* **5171**, 111. DOI. ADS.